Progress in Nuclear Energy 202 (2027) 106620

Contents lists available at ScienceDirect

Progress in Nuclear Energy

journal homepage: www.elsevier.com/locate/pnucene

Assessment of a twisted double-tube latent heat storage system from the perspectives of the first and second laws of thermodynamics throughout the melting and solidification processes

Abderrahmane Aissa [a], Ali Alkhafaji [b], Dheyaa J. Jasim [c], Narinderjit Singh Sawaran Singh [d], Sorour Alotaibi [e], Mahmut Taner [f], Shaghayegh Baghaei [g,*], Soheil Salahshour [h,i,j,k]

[a] Laboratoire de Physique Quantique de La Matière et Modélisation Mathématique (LPQ3M), University of Mascara, Algeria
[b] Advanced Technical College, University of Warith Al-Anbiyaa, Karbala, Iraq
[c] College of Engineering, University of Al Maarif, Al Anbar, 31001, Iraq
[d] Faculty of Data Science and Information Technology, INTI International University, Persiaran Perdana BBN, Putra Nilai, Nilai, 71800, Malaysia
[e] Mechanical Engineering Department, College of Engineering and Petroleum, Kuwait University, P.O. Box 5969, Safat, 13060, Kuwait
[f] Faculty of Engineering and Architecture, Istanbul Gelisim University, Istanbul, Türkiye
[g] Fast Computing Center, Shabihsazan Ati Pars, Tehran, Iran
[h] Faculty of Engineering and Natural Sciences, Istanbul Okan University, Istanbul, Turkey
[i] Faculty of Engineering and Natural Sciences, Bahcesehir University, Istanbul, Turkey
[j] Research Center of Applied Mathematics, Khazar University, Baku, Azerbaijan
[k] Faculty of Science and Letters, Piri Reis University, Tuzla, Istanbul, Turkey

ARTICLE INFO

Keywords:
Frictional entropy generation
Latent heat storage system
Phase change material
Thermal entropy generation
Twisted tube
Energy Efficiency

ABSTRACT

The current study numerically investigates the impact of twist angle on the performance of a twisted double-tube latent heat storage (LHS) system, evaluating first- and second-law efficiencies during melting and solidification. Water serves as the heat transfer fluid (HTF) circulating within the inner tube, while the phase change material (PCM) RT35 is situated in the annular space. Performance is evaluated by examining the PCM temperature, liquid fraction, and the rates of thermal and frictional entropy generation over time. The findings indicate that lower twist angles result in reduced melting and solidification durations. A notable exception is the 360° case during melting, which achieves the shortest melting time among all configurations due to the dominance of vortex-enhanced convective heat transfer over the minor stagnation-zone penalty at this twist angle. Frictional entropy generation is consistently negligible compared to thermal entropy generation. Thermal entropy generation exhibits an increasing-then-decreasing trend during solidification, with peak values of 7.8 $W/m^3/K$ and 1.8 $W/m^3/K$ recorded during solidification and melting, respectively. At higher twist angles, both phase-change durations are extended.

1. Introduction

Fossil fuels account for a significant portion of the world's current energy requirements (Cîrstea et al., 2018). The difficulties associated with fossil fuel usage have compelled communities to seek renewable energy alternatives (Yan et al., 2021). Consequently, the development of energy-conversion systems to capture energy from renewable sources is essential. Solar energy, recognized as the most promising clean thermal energy source, is intermittent, making its utilization heavily dependent on energy storage systems. Thermal energy storage (TES) systems can be categorized into three types: sensible TES (STES), latent TES (LTES), and thermochemical TES. In the case of LTES, thermal energy is stored within a phase change material (PCM) (Khedher et al., 2025) (Khedher et al., 2024) (Khedher et al., 2023) . Although LTES offers advantages such as consistent temperature-controlled heat storage and release and high energy storage density, its implementation is primarily hindered by the low thermal conductivity of PCMs. To address this limitation, various techniques have been applied in LTES systems, including embedding solid porous materials within PCMs, utilizing fins (both longitudinal and radial), and employing specially designed contact

* Corresponding author.
E-mail addresses: a.aissa@univ-mascara.dz (A. Aissa), shaghaieghbaghaie@yahoo.com (S. Baghaei).

https://doi.org/10.1016/j.pnucene.2026.106620
Received 24 September 2025; Received in revised form 7 April 2026; Accepted 13 September 2026
Available online 23 September 2026
0149-1970/© 2026 Elsevier Ltd. All rights are reserved, including those for text and data mining, AI training, and similar technologies.

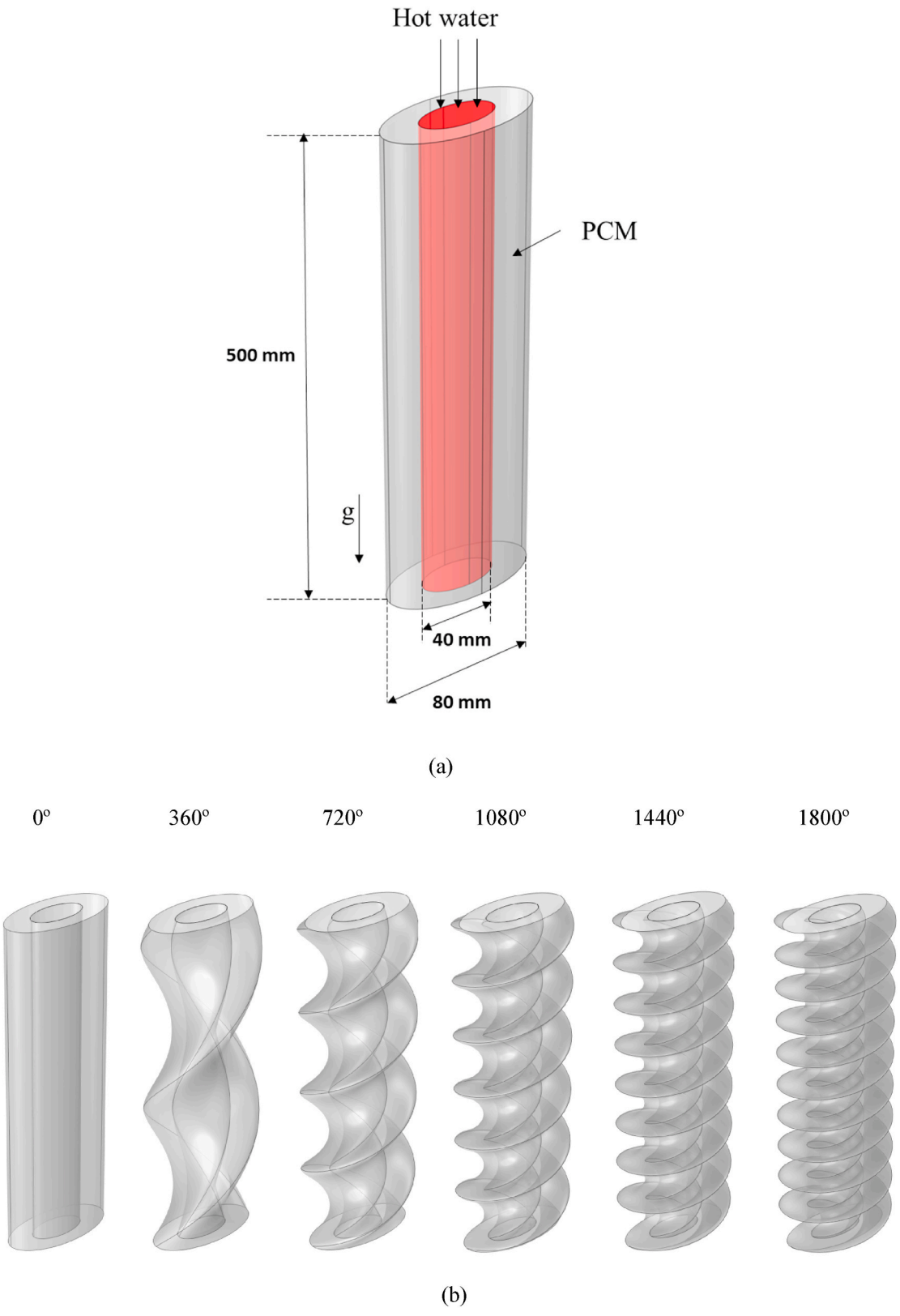


Fig. 1. (a) Twisted double-tube LHS system considered in this work and (b) cases with different twist angles.

surfaces, such as zig-zag (Talebizadehsardari et al., 2021), twisted fins (Song et al., 2021), and tree-shaped fins (Huang et al., 2022). Beyond geometrical modifications, recent studies have also explored operational strategies, such as rapid charging and discharging cycles, to enhance system performance (Huang et al., 2025a) further. Numerous studies have explored the impact of using longitudinal (Wang et al., 2016; Pizzolato et al., 2017; (Boujelbene et al., 2024) 2018; Mahdi et al., 2018, 2019) and radial fins (Hosseini et al., 2015; Yang et al., 2017; Yuan et al., 2016) during melting and solidification processes. Shokouhmand and Kamkari (2012) investigated the melting process of

Table 1
Thermophysical properties of RT35 (Dehkordi et al., 2015; GmbH).

Property	ρ [kg/m^3]	L_f [kJ/kg]	C_p [kJ/kg.K]	k [W/m.K]	μ [N.s/m^2]	T_L [K]	T_S [K]	β [1/K]
Values	815	170	2.0	0.2	0.023	309	302	0.0006



Fig. 2. A view of the employed grid.

Table 2
Validation outcomes.

Time (s)	Mean PCM liquid fraction		Mean PCM temperature (K)	
	Present	Ref. (Eisapour et al., 2021)	Present	Ref. (Eisapour et al., 2021)
101	0.104	0.102	302.591	301.735
465	0.341	0.338	306.501	305.88
826	0.539	0.536	311.124	310.506
1153	0.689	0.690	318.154	318.699
1504	0.744	0.740	326.321	325.639
2967	0.815	0.818	329.443	330.651
4428	0.870	0.873	331.547	332.289
6681	0.931	0.934	333.726	334.217
8267	0.959	0.964	334.776	335.181
10487	0.996	0.997	336.111	336.819

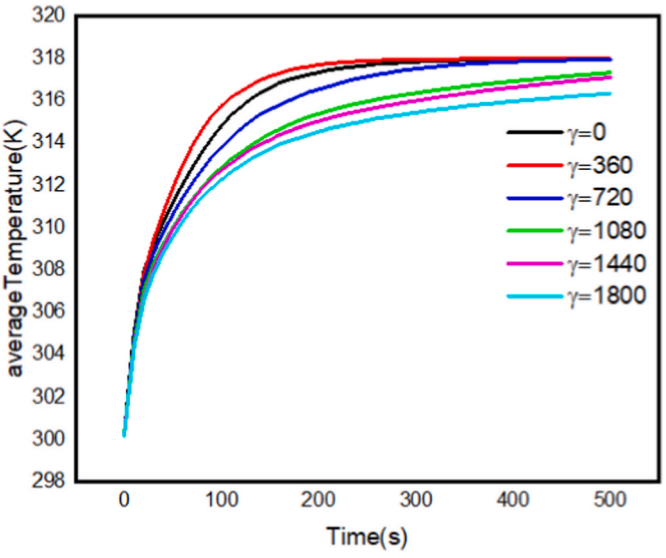


Fig. 3. PCM temperature versus time for different twist angles during the melting process.

PCM in a horizontal latent heat storage (LHS) system fitted with longitudinal fins, demonstrating that the PCM melting rate correlates with the number of fins. The use of circular fins in a TES using $MgCl_2 \cdot 6H_2O$ as the PCM was studied by Choi and Kim (1992). The findings indicate that the use of circular fins resulted in a 3.5-fold enhancement of the convection coefficient. Furthermore, it was noted that the flow rate of the heat transfer fluid (HTF) has a significant influence on the heat transfer rate in the finned unit compared to the non-finned system. From the literature review, it can be inferred that multiple strategies exist to enhance the performance of latent heat storage (LHS) systems by applying single or hybrid techniques in appropriate combinations (Jourabian et al., 2012, 2016, 2020). Various alterations to heat transfer surfaces have been implemented to boost the efficiency of LHS systems (Kalapala and Devanuri, 2018). To increase the heat transfer surface area, zig-zag-shaped surfaces are utilized in thermal energy storage (TES) systems. Wang et al. (2015) examined the impact of zig-zag surface configuration on the melting of phase change material (PCM) within a plate-type heat exchanger. Channel waviness is widely used as a surface modification technique in heat exchangers (Lotfi et al., 2016; Kashani et al., 2012); however, few studies have evaluated its application in LHS systems. The influence of waviness on the contact surfaces of an LHS system during the PCM's solidification phase was investigated by Abdollahzadeh and Esmaeilpour (2015). Their research demonstrated that for varying Grashof numbers and an initial liquid fraction of 0.3, the solidification duration was reduced by 20%. One geometry proposed by researchers to enhance heat exchanger performance is the twisted tube. In an experimental study, Dong et al. (2020) compared the effectiveness of a spiral twisted tube heat exchanger filled with thermal oil and water with that of shell-and-tube heat exchangers featuring ordinary and spiral-groove tubes. The working fluids analyzed for the heat exchangers were thermal oil and water. The effects of mass flow rate, Reynolds number, and inlet temperature of the working fluids on the outcomes were examined. Among the heat exchangers evaluated, the spiral twisted tube heat exchanger was found to exhibit the highest performance. Guo and Wang (2020) numerically inspected the effect of thermal boundary condition (i.e., constant temperature and constant heat flux) on the efficacy of a twisted elliptical tube. They reported that the twisted tube performed better under a constant-temperature boundary condition. Khoshvaght-Aliabadi et al. (2021) numerically compared the performance of helical, serpentine, and Archimedes spiral twisted tubes. The results indicated that the heat transfer rate could be improved by up to 60% with the considered twisted tube compared to a smooth tube. The twisted serpentine tube performed better than the other cases. Li et al. (2021) numerically explored the performance of a twisted hairpin heat exchanger. They found that reducing the twist pitch length and increasing the inner tube aspect ratio could improve the shell-side performance of the heat exchanger. Luo and Song (2021) attempted to enhance the efficiency of a hairpin heat exchanger by utilizing an innovative twisted annulus formed by counter-twisted oval tubes. They reported a 157% improvement in the Nusselt number of twisted annuli compared to that of the plain annuli. Yu et al. (2022) simulated the turbulent flow of water in a twisted oval tube with various twisted tapes, including classic, triple-channel, four-channel, five-channel, perforated, center-cleared, and ribbed twisted tapes. They reported that using a twisted tape inside a twisted tube could augment the Nusselt number by 23.44-35.58%. As a design criterion for energy storage systems, the second law of thermodynamics may also be used alongside the first law. The entropy generation rate characterizes systems from the perspective of the second law. However, there is a scarcity of studies on LHS systems that examine them through the lens of entropy generation (López-Núñez et al., 2020). Erek et al. (Erek and Dincer, 2008) analyzed the performance of a shell-and-tube LHE system from a second-law perspective. They found that the system diameter primarily influenced entropy generation, whereas Reynolds number and tube length did not have a significant impact. Nguyen et al. (2019) investigated the solidification process of nano-PCM integrated within a porous medium under the influence of a magnetic field, with a focus on entropy generation. The findings indicated that the frictional entropy diminished over time; conversely, the thermal entropy exhibited a trend of increasing and then decreasing over the same period. Furthermore, it was noted that higher thermal and frictional entropy generation values corresponded to elevated Reynolds numbers. Shahsavar et al. (2021) conducted an

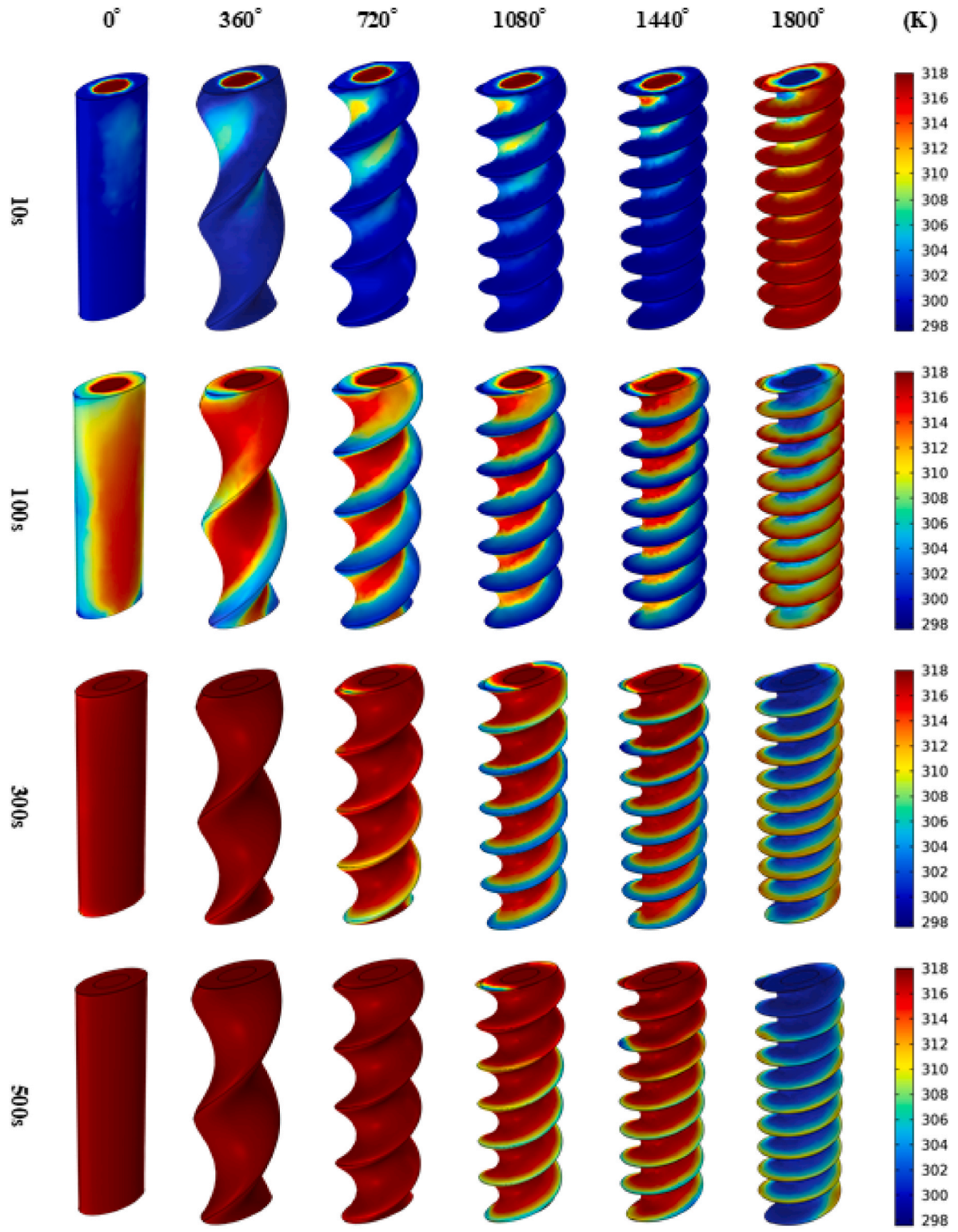


Fig. 4. PCM temperature contours (K) in the melting process for different twist angles and different times.

entropy analysis on a triplex-tube latent heat storage system with wavy channels during both solidification and melting phases. This system was analyzed under varying wave amplitudes, heat transfer fluid (HTF) temperatures, and Reynolds numbers. The results show that an increase in wave amplitude resulted in a reduction in both melting and solidification durations.

The literature review reveals that while considerable research has been devoted to geometric modifications of fins and contact surfaces and to second-law entropy analyses in LHS systems, a critical gap remains: no published study has simultaneously examined the performance of a twisted double-tube LHS system from both first- and second-law perspectives during a complete phase change cycle. While twisted tubes have been shown to enhance convective heat transfer in conventional heat exchangers, their application in PCM-based LTES introduces a fundamentally different trade-off: the same geometric twist that generates beneficial secondary vortical flows on the HTF side also creates

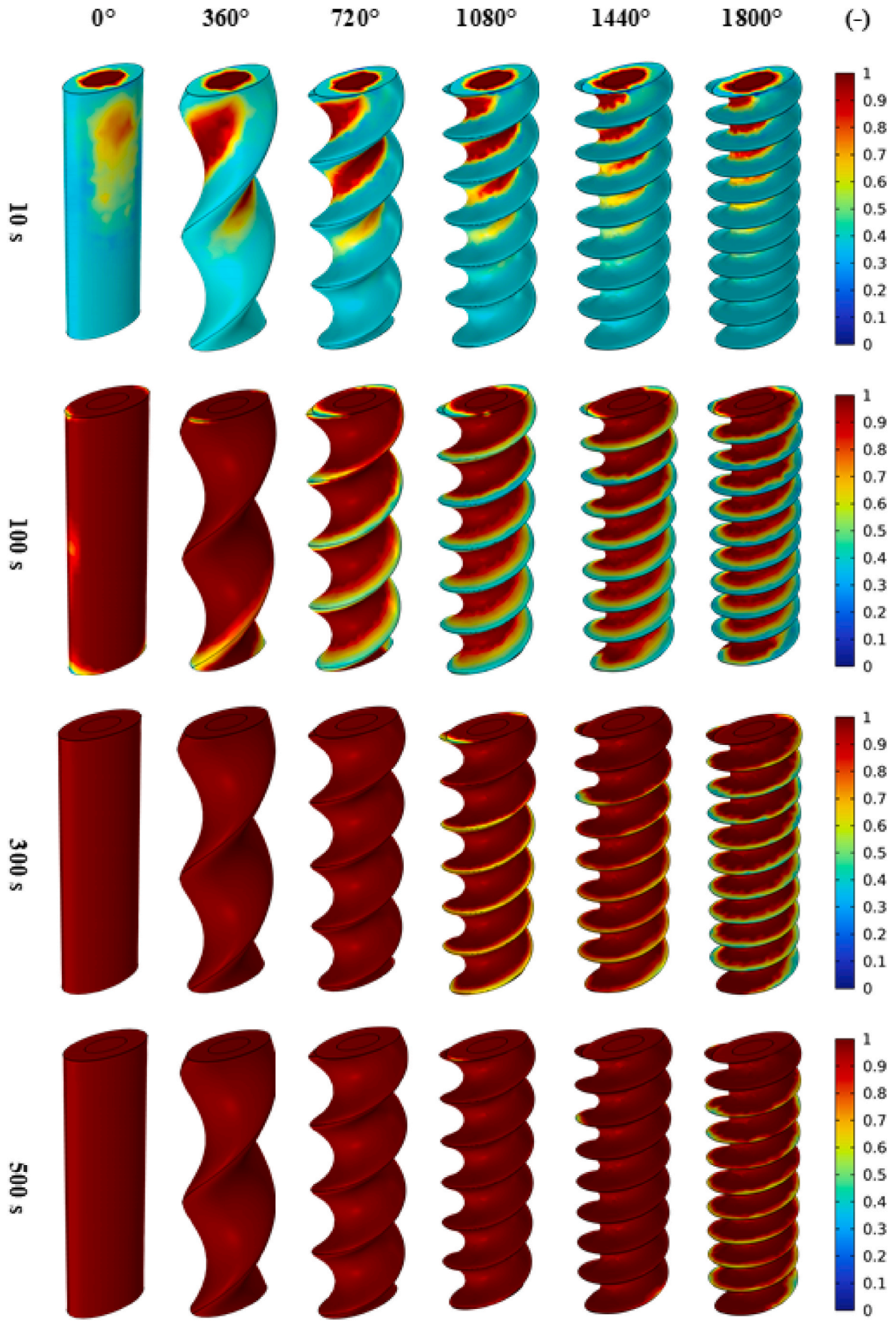


Fig. 5. Contours of PCM liquid fraction at different times and for different twist angles.

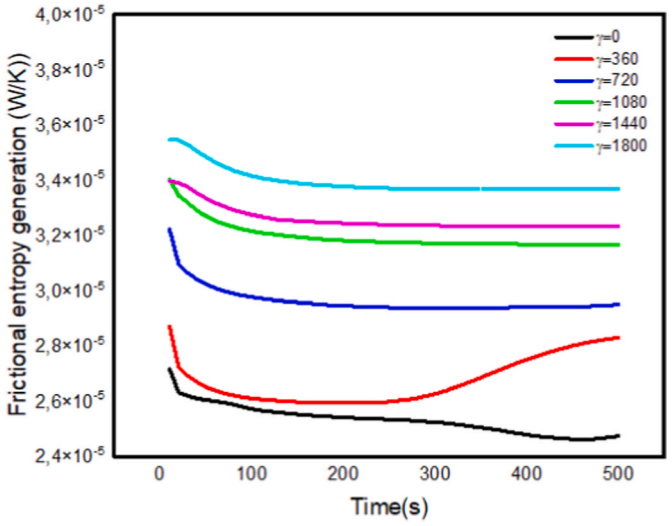


Fig. 6. Overall frictional entropy generation rate versus time during the melting process for different twist angles.

ring-shaped stagnation zones in the PCM annulus, where conduction dominates, and heat transfer is impeded. This coupled competing mechanism, vortex-enhanced heat transfer versus stagnation-zone proliferation, has not been characterized in terms of either phase change kinetics or thermodynamic irreversibilities. Furthermore, the relationship between twist angle and entropy generation during solidification, which involves a fundamentally different heat transfer regime than melting, remains entirely unexplored. The present study addresses this gap by evaluating the performance of a twisted double-tube LHS system under six twist angles (0°, 360°, 720°, 1080°, 1440°, and 1800°) using both first- and second-law analyses. A key outcome is the identification and mechanistic explanation of an optimal twist angle of 360° for melting performance, along with a comprehensive comparative analysis of entropy generation behavior during both charging and discharging.

2. System description

The system under investigation is a vertical double-tube heat exchanger comprising two twisted elliptical tubes with twist angles of 0° (straight tube), 360°, 720°, 1080°, 1440°, and 1800° (see Fig. 1). Water serves as the heat transfer fluid (HTF) within the inner tube, while RT35 is utilized as the phase change material (PCM) in the annular space. RT35 was selected for this numerical study due to its well-documented and stable thermophysical properties, which make it a common reference material in LTES research, facilitating validation and comparison with existing studies (Dehkordi et al., 2015; GmbH). Its melting temperature range (approximately 302–309 K) is suitable for low-to-medium temperature solar thermal energy storage applications, aligning with the broader research background of integrating LTES with renewable energy sources. The thermophysical properties of RT35 are detailed in Table 1.

The heat exchanger is 500 mm long. The inner tube features short and long diameters of 20 mm and 40 mm, respectively, while the outer tube has short and long diameters of 40 mm and 80 mm, respectively. To ensure a fair comparison across all geometries, the following parameters were held constant.

- **Total length:** 500 mm for all cases
- **Cross-sectional area:** The cross-sectional areas of both the inner tube (for HTF) and the annular region (for PCM) are kept constant. The tubes are twisted, but their elliptical profiles (major and minor diameters) remain identical, ensuring the same PCM volume and HTF flow area in all configurations.
- **Operating conditions:** HTF inlet temperature and velocity (Reynolds number), as well as initial PCM temperature, are identical for all cases within each process (melting or solidification).

At the inlet of the inner tube, uniform temperature conditions are maintained (285 K during solidification and 323 K during melting), along with a velocity of 0.039 m/s, corresponding to a Reynolds number of 2000. The outflow boundary condition is applied at the outlet, and the outer tube surface is assumed to be adiabatic. The system's performance is analyzed separately for the charging (melting) and discharging (solidification) processes. During the charging phase, the initial temperature of the PCM is set at 285 K, while in the discharging phase, it is 323 K.

3. Mathematical modeling

It should be emphasized that neglecting close-contact melting and solid settlement simplifies the model and isolates the geometric influence of tube twisting. However, these effects may influence phase interface evolution in practical applications.

Using the enthalpy-porosity method introduced by Brent et al. (1988), the mass conservation and momentum equations in the PCM region could be stated by Eqs (1) and (2), respectively;

$$\frac{\partial \rho}{\partial t} + \nabla . \rho \vec{V} = 0 \tag{1}$$

$$\rho \frac{\partial \vec{V}}{\partial t} + \rho \left(\vec{V} . \nabla \right) \vec{V} = -\nabla P + \mu \left(\nabla^2 \vec{V} \right) - \rho_{ref} \beta \left(T - T_{ref} \right) \vec{g} - \vec{S} \tag{2}$$

where $\vec{V}$ is the velocity vector, P is the pressure, T is the temperature, and $T_{ref} = 293$ K; also, the Boussinesq approximation is used to model the natural convection effect in the momentum equation (Eq. (2)). The source term, $\vec{S}$ in Eq. (2) is defined as:

$$\vec{S} = A_m \frac{(1-\lambda)^2}{\lambda^3 + 0.001} \vec{V} \tag{3}$$

In Eq. (3), A_m is the mushy zone constant whose value is taken as 10^5 (Eisapour et al., 2021; Ye et al., 2011; Assis et al., 2007; Sardari et al., 2019); also, λ is the liquid fraction of the PCM.

The energy equation could be written as Eq. (4) (Shahsavar et al., 2021):

$$\frac{\rho C_p \partial T}{\partial t} + \nabla \left(\rho C_p \vec{V} T \right) = \nabla (k \nabla T) - S_L \tag{4}$$

The source term, S_L in Eq. (4), could be stated as Eq. (5) (Wang et al., 2015);

$$S_L = \frac{\partial \rho \lambda L_f}{\partial t} + \nabla \left(\rho \vec{V} \lambda L_f \right) \tag{5}$$

Where λ is the indicator of the melting situation, which is defined according to Eq. (6) (Al-Abidi et al., 2013);

$$\lambda = \frac{\Delta H}{L_f} = \begin{cases} 0 & if \ \ T < T_{Solidus} \\ 1 & if \ \ T > T_{Liquidus} \\ \dfrac{T - T_{Solidus}}{T_{Liquidus} - T_{Solidus}} & if \ T_{Solidus} < T < T_{Liquidus} \end{cases} \tag{6}$$

Where ΔH is the fractional latent heat of the PCM that may vary between the values of zero and L_f for solid and liquid phases, respectively. It should be noted that the aforementioned governing equations are derived based on the following assumptions (Li et al., 2019):

- Incompressible Newtonian fluid for the PCM in the liquid state.
- No volume expansion of the PCM upon phase change.

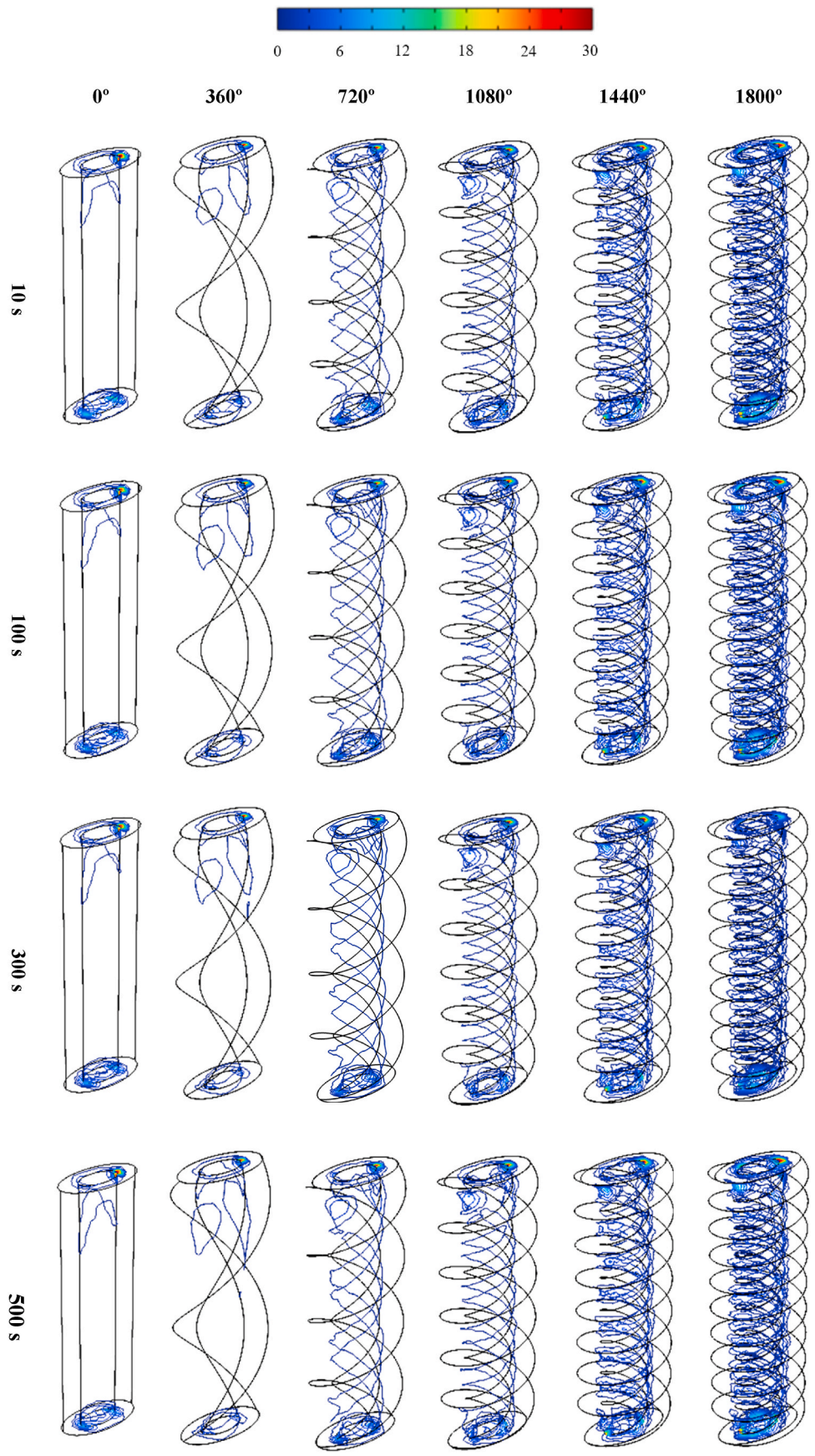


Fig. 7. Contours of frictional entropy generation rate ($\times 10^{-4}$ W/m^3.K) during the melting process at different times and for different twist angles.

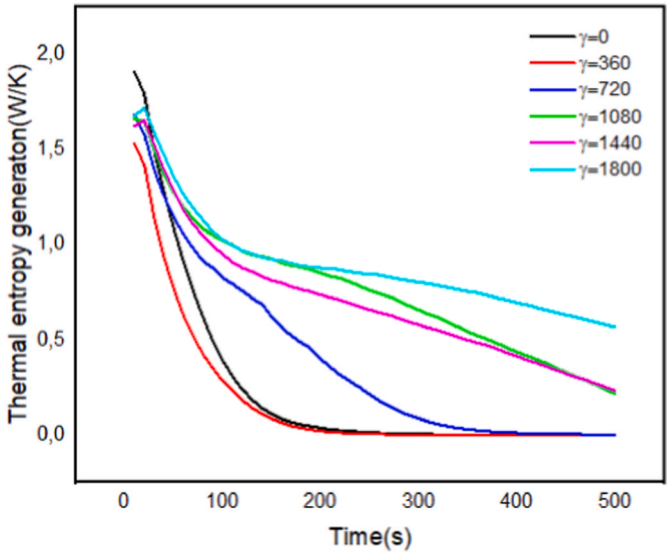


Fig. 8. Overall thermal entropy generation versus time during the melting process for different twist angles.

- No viscous dissipation.
- Constant thermophysical properties of the PCM, except for density in the buoyancy term (Boussinesq approximation).
- The sedimentation of solid-phase PCM due to density differences is not considered. This implies that the model does not account for the close-contact melting phenomenon, in which the solid PCM sinks and comes into direct contact with the heat transfer surface, which can significantly influence melting rate and heat transfer characteristics, particularly in the later stages of melting (Huang et al., 2025b). The current enthalpy-porosity model assumes the solid phase is stationary and forms a fixed porous matrix.
- The flow is laminar and three-dimensional.

The rate of heat storage to or recovery from the PCM could be defined according to Eq. (7) (Xu et al., 2017):

$$\dot{Q}=\frac{Q}{t_m}=\frac{m\left(\int_{solid} c_p dT + L_f + \int_{liquid} c_p dT\right)}{t_m} \approx \frac{m\left(c_p(T_L - T_i) + L_f + c_p(T_e - T_S)\right)}{t_m} \tag{7}$$

Where Q is the heat storage/recovery capacity and t_m is the melting/solidification time duration. Note that for the water flow in the inner tube, the governing equations are the conventional Navier-Stokes equations, which could be achieved by omitting the source terms from Eqs. (2) and (4). The pertinent equations to determine the local thermal (S_T''') and frictional (S_f''') entropy generation rates are provided as follows, respectively (Guelpa et al., 2013; Li et al., 2020):

$$S_T'''=\frac{k}{T^2}\left[\left(\frac{\partial T}{\partial x}\right)^2+\left(\frac{\partial T}{\partial y}\right)^2+\left(\frac{\partial T}{\partial z}\right)^2\right] \tag{8}$$

$$S_f'''=\frac{\mu}{T}\left\{2\left[\left(\frac{\partial v_x}{\partial x}\right)^2+\left(\frac{\partial v_y}{\partial y}\right)^2+\left(\frac{\partial v_z}{\partial z}\right)^2\right] + \left(\frac{\partial v_x}{\partial y}+\frac{\partial v_y}{\partial x}\right)^2+\left(\frac{\partial v_z}{\partial x}+\frac{\partial v_x}{\partial z}\right)^2+\left(\frac{\partial v_y}{\partial z}+\frac{\partial v_z}{\partial y}\right)^2\right\} \tag{9}$$

The global entropy generation rates are obtained by integrating the local values over the entire computational volume V (Guelpa et al., 2013; Li et al., 2020):

$$\dot{S}_T=\iiint_V S_T''' dV \ [\mathrm{W/K}] \tag{10}$$

$$\dot{S}_f=\iiint_V S_f''' dV \ [\mathrm{W/K}] \tag{11}$$

where V denotes the full computational domain, and dV is the volumetric differential element. The triple integral is evaluated over the entire PCM and HTF regions.

4. The numerical procedure and validation

The simulations were conducted using ANSYS Fluent and employed the SIMPLE scheme for discretization, along with the PRESTO and QUICK methods for the pressure and momentum/energy equations, respectively. The convergence criterion for all parameters was set at 10^{-5}. The grid independence analysis was done for the heat exchanger with a twist angle of 1800°. Four grids with 11230, 16830, 22360, and 28790 cells were prepared, and the melting time was calculated for all of them, which were 1017 s, 995 s, 970 s, and 968 s, respectively. A grid with more than 22360 cells (Fig. 2) resulted in a melting time difference of less than 0.5%. Therefore, this mesh size was selected for the simulations. After determining the optimal grid, it was used to investigate the effect of the time step on the heat exchanger's melting time with a twist angle of 1800°. Time steps of 0.5 s, 0.2 s, 0.1 s, and 0.05 s were considered, and the melting times were 987 s, 970 s, 969 s, and 968 s, respectively. Therefore, the time step size was considered to be 0.2 s.

For code validation, a double-elliptical pipe LHS system studied numerically by Eisapour et al. (Brent et al., 1988) was employed. This comparative case features water flowing in the inner elliptical tube and RT35 in the elliptical annulus as PCM, with identical boundary conditions and thermophysical properties to our study. Table 2 presents the mean PCM temperature and liquid fraction, compared with the results of Eisapour et al. (2021) at various time intervals, demonstrating excellent agreement with maximum deviations of less than 1.5%, thereby confirming the accuracy and reliability of our numerical model.

5. Results and discussion

The results are presented from the viewpoints of first- and second-law analyses, explaining the local and average time variations in PCM temperature and PCM liquid fraction, as well as the frictional and thermal entropy generation. Since the complete cycle of a PCM encompasses both charge and discharge stages, the explanations for the melting and solidification processes are presented separately in two subsequent sections.

5.1. The melting process

By directing the hot water flow through the inner tube, the PCM would be heated, and as its temperature increased, heat storage would begin. As the first determining factor in the melting process, the variation of PCM temperature vs. time for the LHS with different twist angles is shown in Fig. 3. As shown, the PCM temperature increases from its initial temperature of 300K in a nonlinear trend; the growth rate is higher at early charge times and decreases over time. For a twist angle of 0° (i.e., straight tube), the PCM temperature has increased by 15 K (from 300 K to 315 K) within 100 s and 3 K (from 315 K to 318 K) during the next charge time (i.e., 400 s). Additionally, except for γ = 360°, at each time, the PCM temperature in the twisted tube is lower than that in the straight tube, and this reduction is further enhanced with higher twist angles. At t = 150 s, the PCM temperature is 313.8, 314, 314.2, 315.8, 316.2 and 317 K for twist angles of 1800°, 1440°, 1080°, 720°, 0° and 360°, respectively. The higher rate of PCM temperature increase during the initial charge time is due to the greater temperature difference

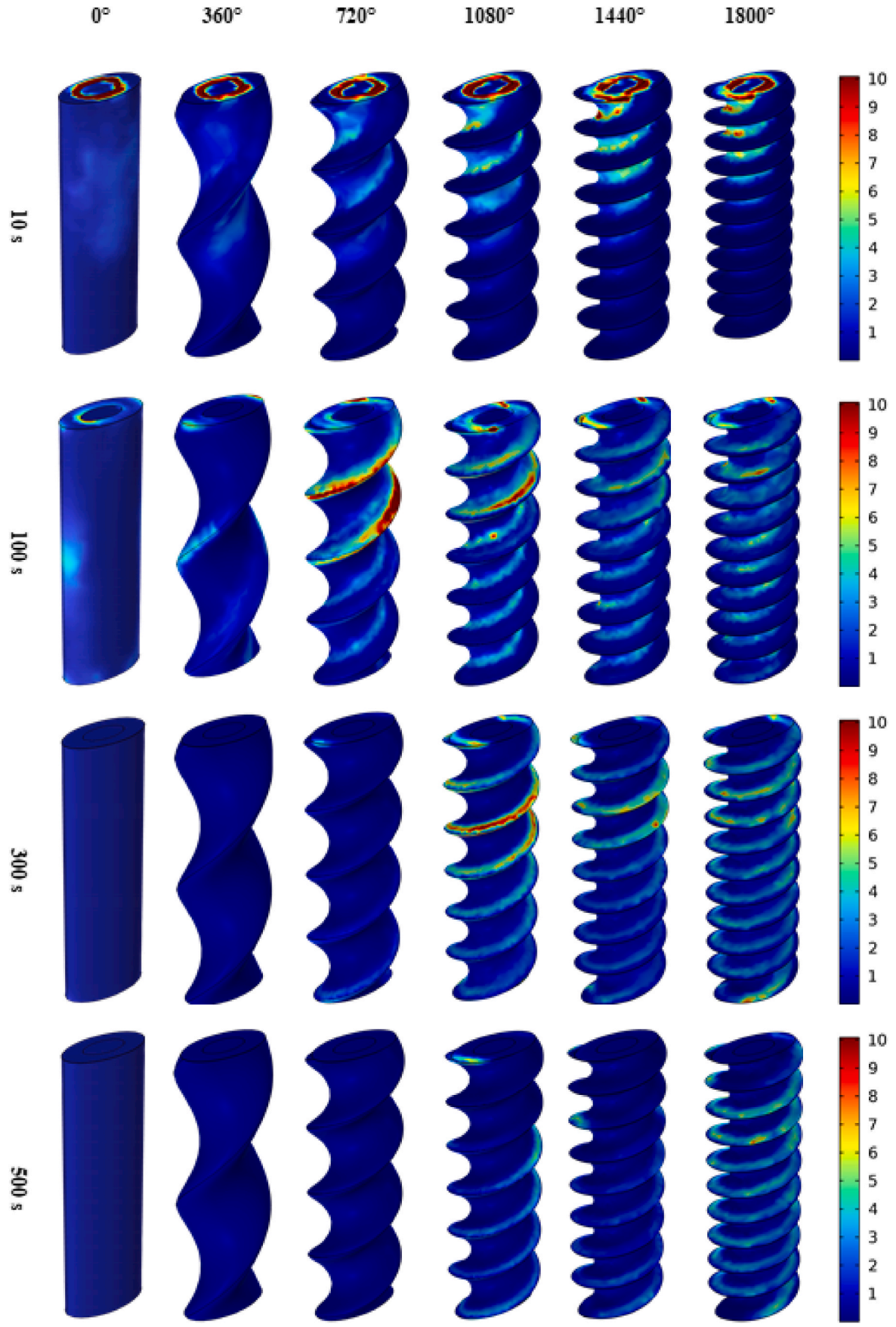


Fig. 9. Contours of thermal entropy generation rate ($W/m^3.K$) during the melting process at different times and for different twist angles.

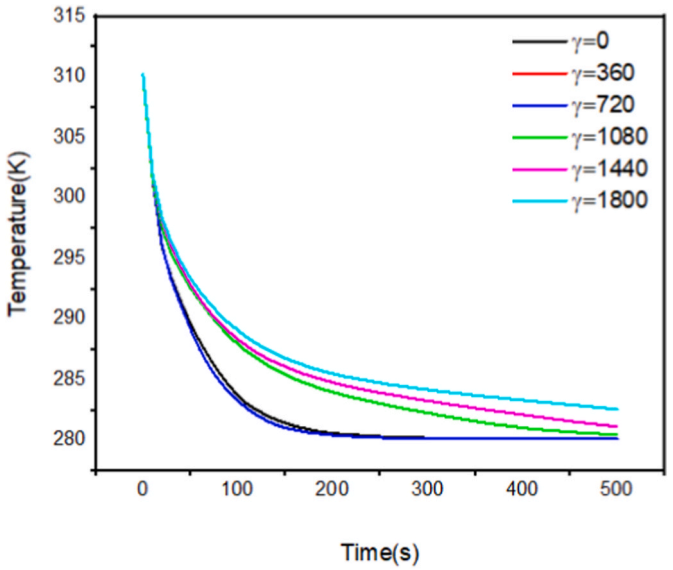


Fig. 10. PCM temperature versus time for different twist angles during solidification.

between the HTF and the PCM. In addition, the decrease in PCM mean temperature with increasing twist angle (except at 360°) results from the development and expansion of static regions. From the static region, we mean the ring-shaped zones with a small volume that result from twisting the cylinder. These static zones, which are not present in the straight cylinder, are formed by twisting the cylinder, and their numbers are increased by increasing the twist angle.

Fig. 4 illustrates the PCM temperature contour for the cylinders with different twist angles at various times during the charge stage. As seen, increasing the twist angle extends the static zone, which has lower temperatures and is indicated by the lighter colors in the figure. In the static zones, the predominant mechanism of heat transfer is conduction; therefore, they are affected minimally by the surrounding hot water temperature. Increasing the number of static zones with their higher-than-melting temperature would decrease the average PCM temperature. It has been verified (Wang et al., 2015) that wavy channels, due to their greater contact area, enhance heat transfer between the HTF and the PCM. Additionally, the generated vortices in the convergent-divergent sections on both the HTF and melted PCM sides enhance heat transfer (Yu et al., 2022). PCM begins to melt from the mid-walls by conduction, and the heat then spreads by natural convection, which ultimately induces liquid PCM circulation and improves the melting process (Hajjar et al., 2020). Due to the gravity direction and the opposite direction of the HTF flow in the inner tube, the melting process terminates at the bottom of the unit. Regarding the 360° case, the twisted tube surface would induce vortical flow on the HTF side, thereby enhancing the heat transfer coefficient. It should be noted that although the vortex flow is present in all other cases as well, the static zones and their decreasing effect on PCM temperature exist at twist angles higher than 360° (720°, 1080°, 1440°, and 1800°). This suggests that the optimal operating condition for achieving the highest PCM temperature during melting is with a 360° twisted tube. The higher the PCM temperature, the higher the fraction of PCM that would be melted.

By inspecting the contour of the PCM melting fraction as in Fig. 5, it is revealed that for the case of a straight tube, the whole PCM would be melted after 300 s from the beginning of the charge process. However, this result is repeated for a twisted tube of 360°; the time required for complete melting increases with the twist angle. This could be explained by increasing the static zones at higher twist angles, which, as described before, reduces the effective heat transfer between the HTF and PCM.

5.1.1. *Mechanistic analysis of the 360° optimal case*

Among the studied configurations, the 360° twisted tube achieves the shortest melting time, a result that appears to contradict the general trend of increasing melting time with increasing twist angle. This section provides an in-depth mechanistic explanation from the perspectives of flow field structure, secondary flow intensity, and stagnation zone distribution. From a flow field standpoint, the 360° twist introduces a mild but coherent helical deformation of the HTF flow path. This deformation generates secondary vortical flows (Dean-type vortices) on the HTF side, which enhance the convective heat transfer coefficient at the HTF-wall interface. Critically, the PCM-side geometry at 360° features only one full rotation over the 500 mm tube length, which is insufficient to generate a significant number of isolated ring-shaped stagnation zones in the PCM annulus. These conduction-limited stagnation zones, which have locally lower temperatures than the bulk PCM, are the dominant thermal resistance at higher twist angles. Inspection of Fig. 4 at $t = 10$ s confirms this: the 360° case exhibits the warmest PCM temperature near the inner tube surface among all cases, consistent with the highest convective driving force, while the characteristic cool stagnation-zone rings visible at 720° and above are absent. This behavior can be understood through a competing-mechanism framework: at low twist angles, vortex-enhanced convection dominates, accelerating melting; at high twist angles (≥720°), the stagnation-zone proliferation effect dominates, impeding melting. The 360° case sits at the crossover optimum where the vortex benefit is maximized before stagnation zones begin to proliferate. As shown in Fig. 5, the liquid fraction at $t = 100$ s is visibly higher for the 360° and 0° cases than for any twisted case with $\gamma \geq 720°$, confirming faster melting. The 360° configuration thus represents a geometric optimum for the charging process: the induced secondary flow enhances convective heat transfer without incurring the penalty of stagnation zones.

From a second-law perspective (Fig. 8), the 360° case displays the lowest thermal entropy generation rate throughout the melting process, a direct consequence of the smallest temperature gradient between the HTF and PCM. This confirms that the 360° configuration is not only the fastest melter but also the most thermodynamically efficient configuration during charging. The anomalous behavior is therefore not a contradiction of the general trend, but rather a physically expected optimum arising from the balance between two competing geometric effects.

The rate of entropy generation is a measure of the irreversibilities involved in a process. The irreversibilities during the phase change of PCM are caused by two factors: the heat transfer via the temperature difference between the PCM and HTF (Eq. (8)) and the friction (Eq. (9)). The time variation of the overall frictional entropy generation rate during the charge process is shown in Fig. 6. The overall changes in frictional entropy generation for the assessed cases, except for $\gamma = 360°$, are decreasing. For example, from the beginning to the end of the melting process, the global frictional entropy generation rate decreases by 9.3% and 5.6% (from 2.7×10^{-5} W/K to 2.45×10^{-5} W/K and from 3.55×10^{-5} W/K to 3.35×10^{-5} W/K) for the cases of twist angles of 0° and 1800°, respectively. The greater frictional entropy generation at the beginning of the melting process can be attributed to the higher velocity gradients during this time.

The contours of frictional entropy generation at different times and for different twist angles are shown in Fig. 7. The prevailing trend of frictional entropy generation over time is increasing for all the studied cases, except for the case of $\gamma = 360°$, which exhibits a decreasing-increasing trend over time. This could be attributed to the increase in the PCM liquid fraction and the generation of natural convection after $t = 300$ s. By increasing the velocity in the PCM zone and the resulting velocity gradients, the frictional entropy would grow accordingly. It is worth noting that a similar situation occurs in the other cases, which occur later than 300s and cannot be seen at this time interval. This illustrates the exceptional case of a twisted tube with $\gamma = 360°$. Another point observed in Figs. 6 and 7 is that the frictional entropy generation

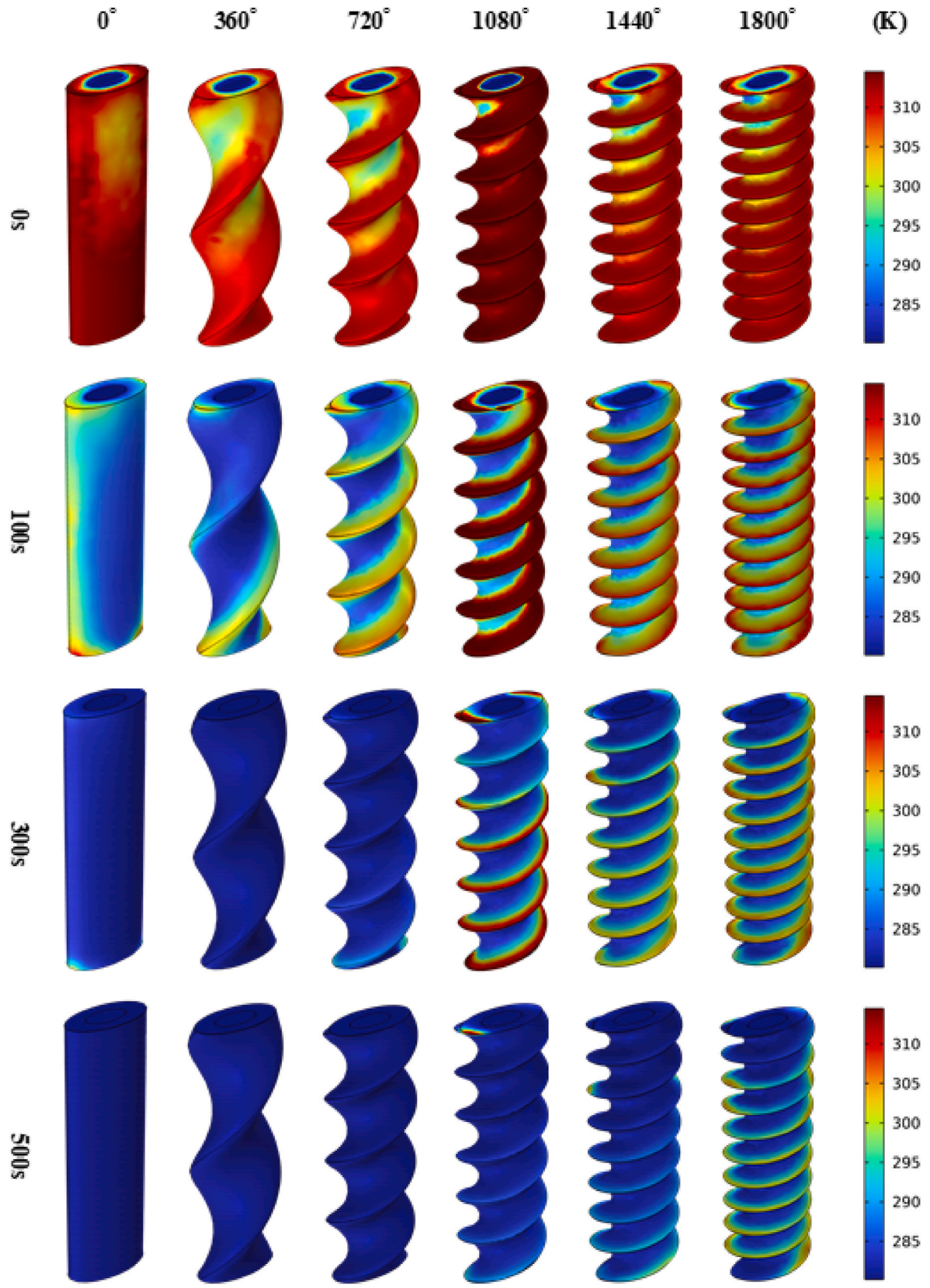


Fig. 11. PCM temperature contours (K) in the solidification process for different twist angles and different times.

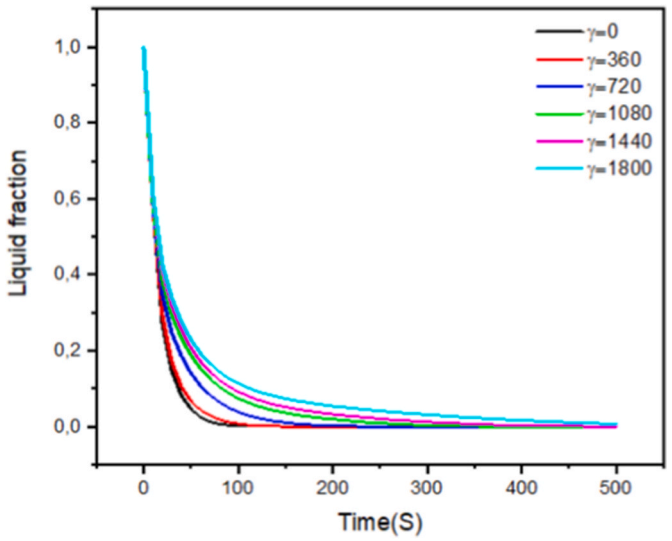


Fig. 12. PCM liquid fraction versus time for different twist angles during the solidification process.

rate increases with increasing twist angle. The global entropy generation for the straight tube ($\gamma = 0°$) and twisted tube ($\gamma = 1800°$) is 2.55×10^{-5} W/K and 3.41×10^{-5} W/K, respectively, which indicates a 34% increase in entropy generation when the straight tube is twisted. The higher frictional entropy generation rate at higher twist angles can be attributed to the increased static zones that result from them.

Like the frictional entropy generation rate, the thermal entropy generation rate decreases over time, but with a steeper decline (Fig. 8). From the beginning to the end of the melting process, the thermal entropy generation rate reduces by 97% and 63% (from 1.8 W/K to 0.05 W/K and from 1.75 W/K to 0.65 W/K) for twist angles of 0° and 1800°, respectively. The higher declination rate of thermal entropy generation than that of frictional entropy generation is due to the strong dependence of thermal entropy generation on the temperature gradient between the PCM and HTF. As the PCM temperature increases and approaches its melting point, the rate of thermal entropy generation decreases. Additionally, it is observed that at the end of the examination time (t = 500s), the PCM average temperature is the highest for the cases of $\gamma = 0°$, 360°, and 720°, where the thermal entropy generation simultaneously reaches zero. Still, for the other cases, the PCM temperature is lower, and also, the thermal entropy generation is higher. The highest rate of thermal entropy generation occurs for the highest twist angle (i.e., $\gamma = 1800°$), and the lowest for $\gamma = 360°$. Increasing the thermal entropy generation by increasing the twist angle results from expanding the static zone where the low-temperature PCM exists and reducing the PCM's mean temperature. The overall change of the thermal entropy generation rate by the rise of twist angle is increasing except for the case of $\gamma = 360° \ °$ for which the thermal entropy generation is less than that of the straight tube (i.e., $\gamma = 0°$). This different behavior can be attributed to the higher PCM temperature during melting in this case, compared to the others, which ultimately decreases the temperature gradient and the rate of thermal entropy generation (Fig. 9). By inspecting the rates of frictional and thermal entropies, it is found that, in all the studied cases, the frictional entropy rate is negligible compared to the thermal entropy rate.

5.2. The solidification process

The discharge process begins by directing the cold water through the inner tube. By releasing the stored heat to the HTF, the PCM temperature decreases, and solidification begins.

The time variation of PCM temperature during the solidification process is depicted in Fig. 10. Although the PCM temperature decreases during solidification, the rate of decline varies across the examined cases. The PCM temperature decline rate is higher at low twist angles and decreases more quickly, whereas at higher twist angles it decreases more slowly. After 200 s from the beginning of solidification, the PCM temperature decreases by 9.7% (from 310 K to 280 K) for the straight tube ($\gamma = 0°$) and by only 7.4% (from 310 K to 287 K) for the 1800° twisted tube. The lower temporal mean temperature change in cases of higher twist angles is attributable to the presence of static zones. During heat release, the ring-shaped areas around the tube solidify more slowly. In the static zones of PCM, the dominant mode of heat transfer is conduction; therefore, the PCM loses the stored heat over a longer period. This indicates that the ring-shaped areas do not accelerate heat transfer, but rather lengthen the process of heat release.

Importantly, unlike the melting process, where the 360° case achieves the fastest response due to vortex-enhanced convection during solidification, the convective enhancement is limited because the PCM progressively solidifies, suppressing natural convection. Consequently, a monotonic decrease in performance with increasing twist angle is observed throughout the solidification process, without the anomalous 360° behavior observed during melting. Inspection of Fig. 11 confirms this: at t = 10 s, all cases begin at nearly identical temperatures, but by t = 300 s, the high-angle cases (1440° and 1800°) retain noticeably higher temperatures in the stagnation zones.

5.2.1. PCM liquid fraction during solidification

The foregoing discussion can also be justified by inspecting the PCM liquid fraction versus time (Fig. 12). At higher twist angles, the liquid fraction is higher at each time; also, the difference between the liquid fractions is greater at the initial times of the solidification process and decreases over time. At t = 50 s and t = 400 s, by using the 1800° twisted tube instead of the straight tube, the liquid fraction grows by 570% and 100% (from 0.03 to 0.2 and from 0.01 to 0.02), respectively. This indicates that the effect of using a twisted tube instead of a straight tube is higher at the initial stages of the solidification process and diminishes over time.

The spatial evolution of the liquid fraction is visualized in Fig. 13. For twist angles below 720°, there is no noticeable change in PCM temperature (Fig. 10) or liquid fraction; the major change occurs at twist angles above 720°. This threshold behavior has important practical implications: moderate twist angles (≤360°) offer enhanced HTF-side heat transfer during melting without significantly penalizing the solidification rate.

5.2.2. Entropy generation during solidification

After examining the PCM temperature and liquid fraction, the variation of entropy generation is reviewed. The rate of entropy generation is divided into frictional and thermal components, whose time variations are depicted in Figs. 14 and 15, respectively. Here, like in the melting process, the rate of frictional entropy generation is very low compared to that of the thermal entropy generation. The low values of frictional entropy generation are due to the dominant heat transfer mode, natural convection, which results in low velocity gradients.

In contrast to melting, frictional entropy generation increases over time during solidification (Fig. 14). The initial increase is due to the formation of a thin solid layer adjacent to the inner liquid phase, which generates a high velocity gradient at the solid–liquid interface. Although the overall trend is increasing, most of the growth occurs at the beginning of the solidification process (the first 200 s), after which it reaches a near-constant value. Because of the PCM's low thermal conductivity, the solidification process proceeds slowly, and the frictional entropy is still nonzero at t = 500 s. The rate of frictional entropy generation is highest for the highest twist angle and decreases as the twist angle is reduced — attributable to the more intense natural convection within the slowly-solidifying ring-shaped stagnation zones (Fig. 16). In this way, in cases of twisted tubes, the highest value of frictional entropy generation

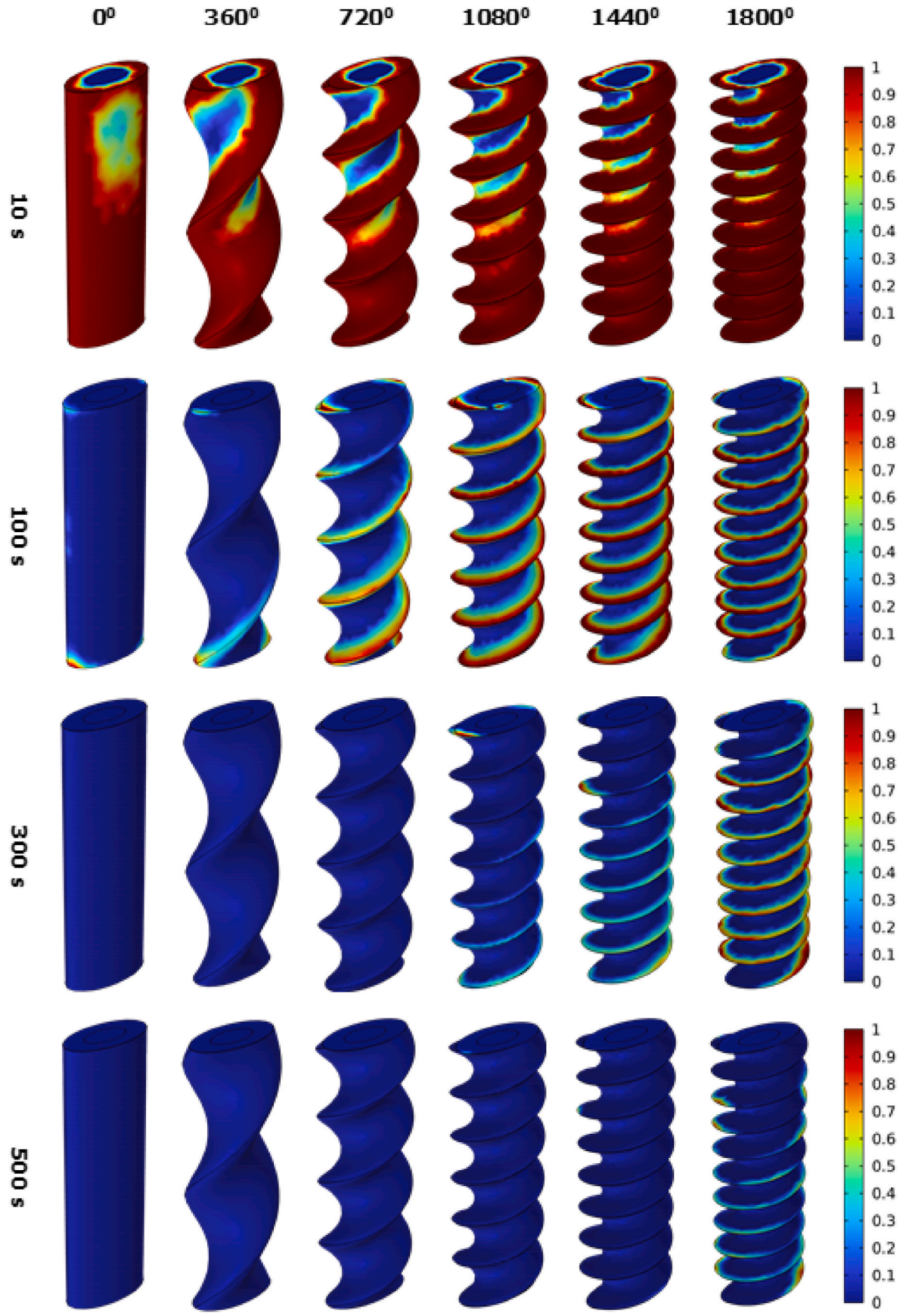


Fig. 13. PCM liquid fraction contours in the solidification process for different twist angles and different times.

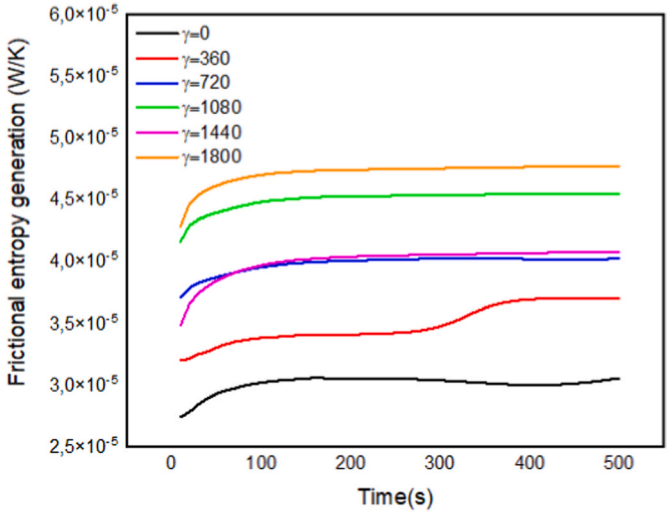


Fig. 14. Overall frictional entropy generation versus time during the solidification process for different twist angles.

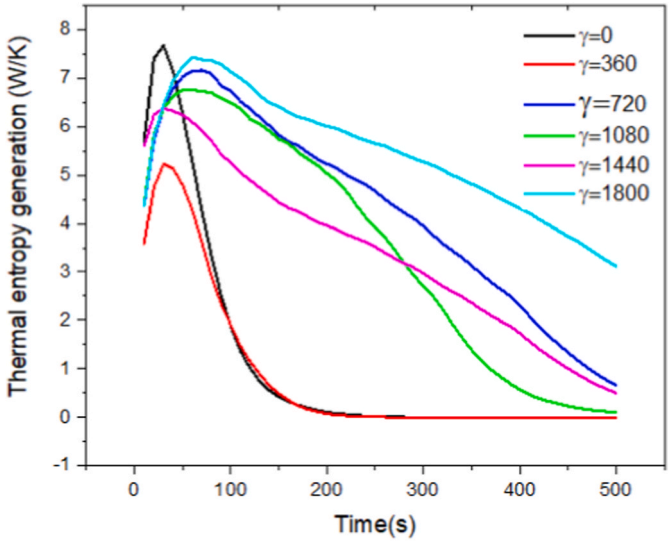


Fig. 15. Overall thermal entropy generation versus time during the solidification process for different twist angles.

occurred within the ring-shaped zones.

The time variation of thermal entropy generation rate for the different studied cases during the solidification process is illustrated in Fig. 15. An increasing-decreasing trend in thermal entropy generation is evident for all cases. At the beginning of solidification, the PCM adjacent to the cold wall solidifies first, forming a thin solid layer. This thin layer beside the melted PCM generates a temperature gradient, thereby increasing the rate of thermal entropy generation. The stored heat inside the liquid PCM is conducted through this layer, and the thickness of the solid layer rises over time. Increasing the solid layer near the wall decreases the velocity gradient and thermal entropy generation rate. Due to the lack of solid PCM in the core area, the thermal entropy generation remains zero there (Fig. 17). Concurrent with the decrease in near-wall temperature, the solid zone area increases, and the dominant heat transfer mode shifts from natural convection to conduction. By proceeding with the solidification process and maintaining a uniform temperature within the PCM, the temperature gradient is reduced, thereby decreasing the rate of thermal entropy generation. This declination trend persists until the endpoint of the solidification process, at which point the thermal entropy generation declines to zero.

The peak thermal entropy generation rate during solidification (approximately 7.8 W/K) is roughly four times that during melting (approximately 1.8 W/K), reflecting the larger temperature gradients that develop during the rapid initial solidification phase. Higher twist angles consistently produce higher peak thermal entropy generation and a longer time to return to zero. The 360° case produces the lowest peak thermal entropy generation during solidification, analogous to its optimal behavior during melting.

5.3. Comparative analysis: melting vs. solidification

A comparison of the twist angle regulation mechanism between the melting and solidification processes reveals several important asymmetries. First, the anomalous 360° optimum is unique to the melting process. During solidification, the performance trend is monotonic: higher twist angles consistently result in slower heat release and higher entropy generation. This asymmetry arises because natural convection, which amplifies the vortex-enhancement effect, is most active during melting and progressively suppressed as solidification advances. Second, frictional entropy generation exhibits opposite temporal trends in the two processes: decreasing during melting (as the growing liquid fraction smoothes velocity gradients) and increasing during solidification (as the solid–liquid interface sharpens velocity gradients). Third, the absolute magnitude of thermal entropy generation is significantly higher during solidification (peak 7.8 W/K vs. 1.8 W/K), indicating that solidification is inherently less thermodynamically efficient. Fourth, the water pressure drop increases monotonically with twist angle from 1.52 Pa (0°) to 2.61 Pa (1800°), a 71.71% increase, and this penalty must be weighed against the thermal performance benefits when selecting the optimal twist angle.

At the end of this section, it is worth noting that the change in water pressure drop with twist angle is another parameter that can influence the selection of the optimal LTES. Because in all simulations, the Reynolds number and thermophysical properties of water are considered constant, therefore, firstly, the water pressure drop is only a function of the twist angle. Secondly, the water pressure drop during melting and solidification does not differ for the same twist pitch. According to the results, the pressure drop of the water flow inside the inner twisted tube with twist pitches of 0°, 360°, 720°, 1080°, 1440°, and 1800° is 1.52 Pa, 1.94 Pa, 2.11 Pa, 2.23 Pa, 2.42 Pa, and 2.61 Pa, respectively. Therefore, the use of the twisted tube with twist pitches of 360°, 720°, 1080°, 1440°, and 1800° results in increases in pressure drop of 27.63%, 38.82%, 46.71%, 59.21%, and 71.71%, respectively.

6. Conclusion

The twisted double-tube latent heat storage system is evaluated from the viewpoints of the first and second laws of thermodynamics during both melting and solidification. The effect of twist angle on the local and global thermal and frictional entropy generation rates, as well as the liquid fraction and temperature distribution of PCM, is analyzed comprehensively. The following results could be drawn from this study.

- In all the studied cases, the generation rate of frictional entropy is lower than that of thermal entropy.
- The melting and solidification times increase with increasing twist angle. The exception is in the melting process for a twist angle of 360°, which has the lowest melting time among the other cases.
- For both the melting and solidification processes, the thermal entropy generation decreases over time in all the studied cases; however, the rate of decline decreases as the twist angle increases.
- The generation rate of frictional entropy reaches a higher value at a very early stage of both solidification and melting, then declines to zero with a near-zero rate of decline.

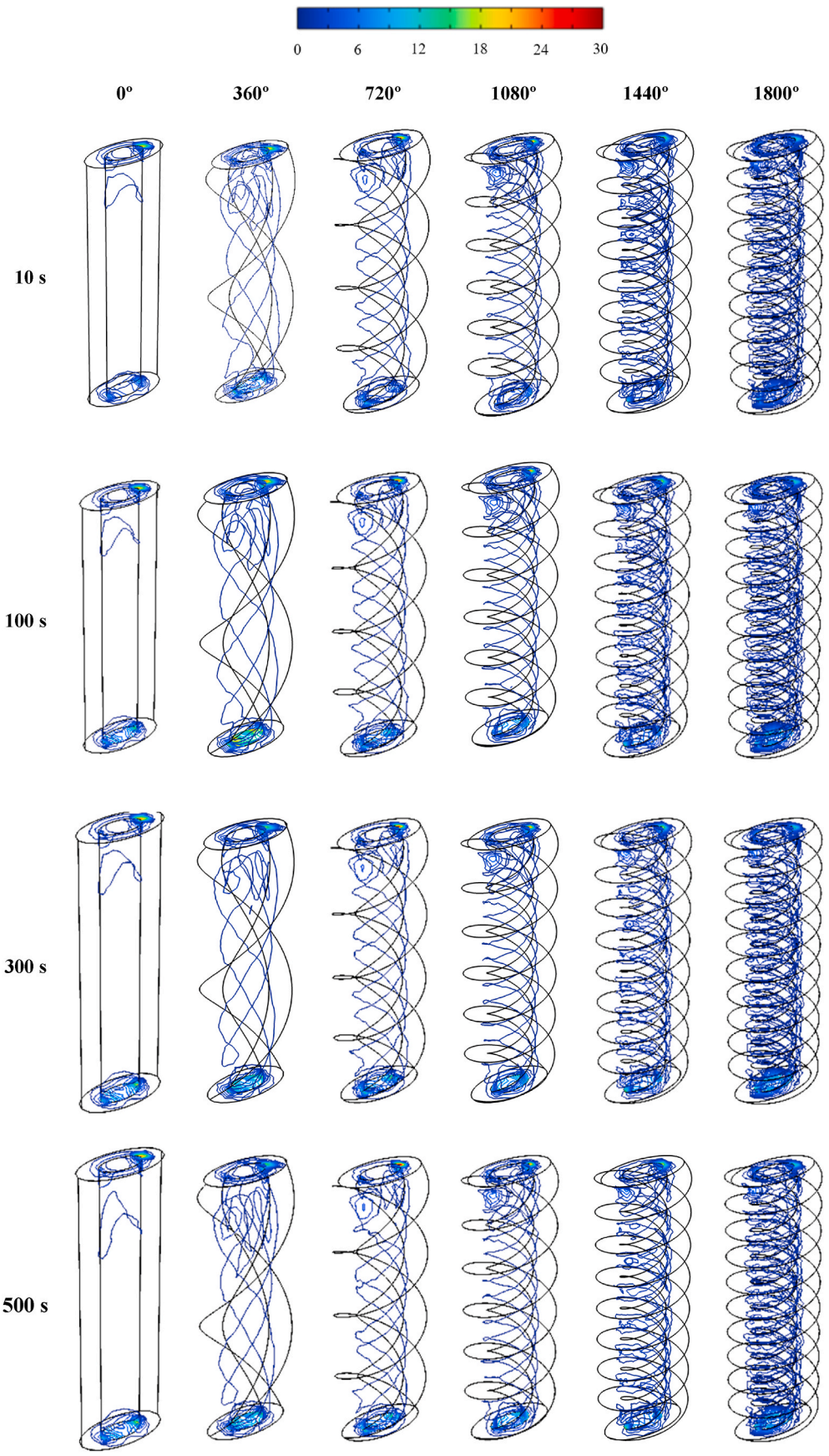


Fig. 16. Contours of frictional entropy generation rate ($\times 10^{-4}$ W/m^3.K) during the solidification process at different times and for different twist angles.

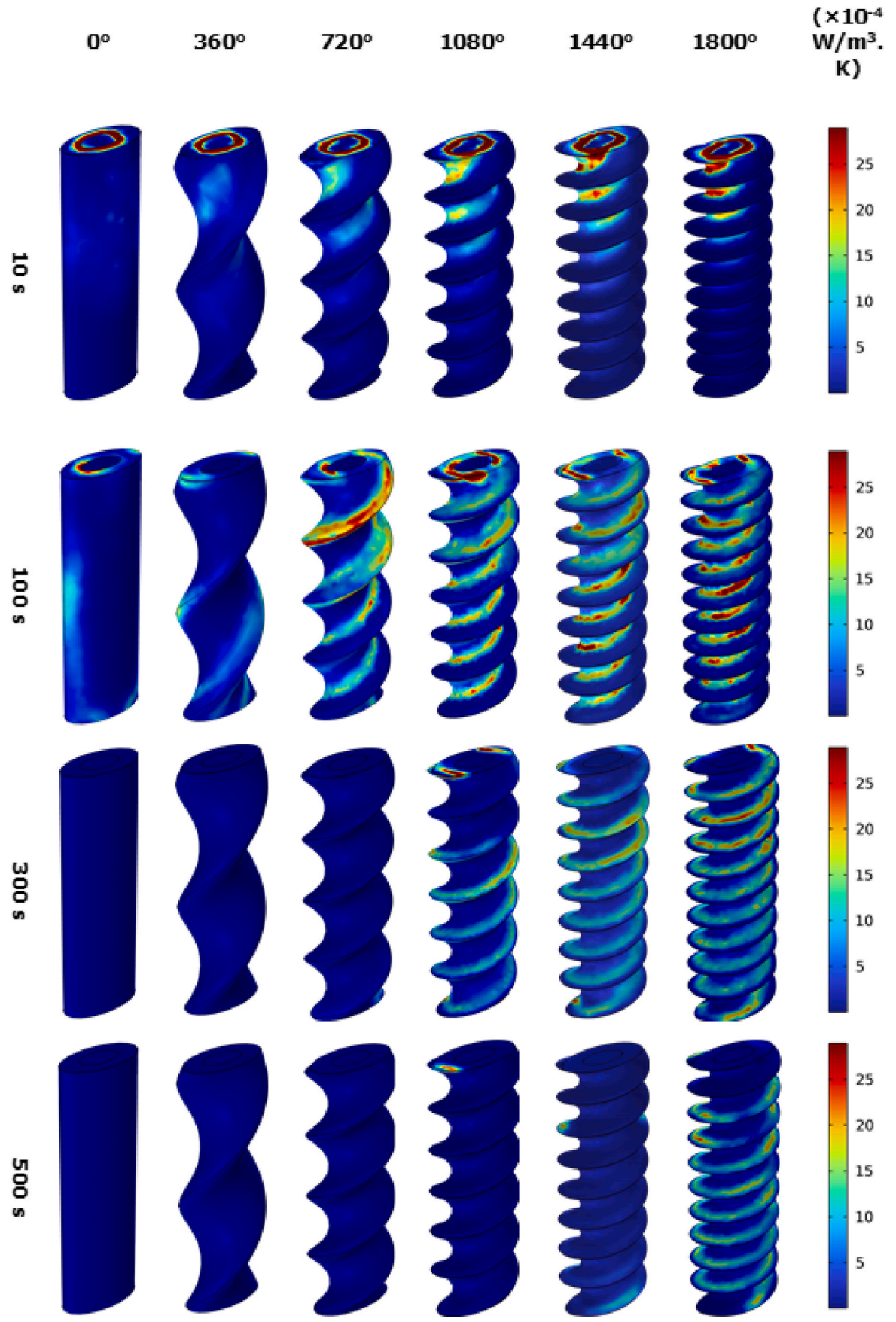


Fig. 17. Contours of thermal entropy generation rate ($\times 10^{-4}$ W/m^3.K) during the solidification process at different times and for different twist angles.

7. Limitations of this study

The present study is subject to several modeling assumptions. First, the enthalpy-porosity model assumes a stationary solid phase and does not account for close-contact melting or solid PCM sedimentation, which may influence phase interface evolution in practical applications. Second, volume expansion upon phase change is neglected. Third, all simulations are performed at a single Reynolds number (Re = 2000, in the laminar regime); the optimal twist angle may differ under turbulent flow conditions. Fourth, only a single PCM (RT35) was investigated; the generalizability of the 360° optimum to other PCMs remains to be verified. Fifth, the outer tube surface is assumed adiabatic, neglecting realistic heat losses.

Engineering Design Recommendations: Based on the findings of this study, the following guidance is provided: (a) For applications where charging speed is the primary objective, a twist angle of 360° is recommended. This configuration achieves the shortest melting time while incurring only a 27.63% increase in pressure drop — the lowest penalty among all twisted configurations. (b) For applications requiring extended heat retention or controlled slow discharge, higher twist angles (1080°–1800°) are appropriate, as their stagnation zones act as thermal buffers; however, the substantially increased pressure drop (47–72%) must be accounted for. (c) For balanced charge-discharge performance with minimal pressure penalty, the 360° geometry represents the overall optimum. (d) When pumping energy is constrained, the straight tube (0°) remains competitive, achieving equivalent melting performance to the 360° case without any pressure drop penalty.

CRediT authorship contribution statement

Abderrahmane Aissa: Methodology, Investigation, Funding acquisition, Formal analysis, Data curation, Conceptualization, Writing – original draft. **Ali Alkhafaji:** Formal analysis, Data curation, Conceptualization, Writing – original draft, Writing – review & editing, Software, Validation. **Dheyaa J. Jasim:** Conceptualization, Writing – original draft, Writing – review & editing, Software, Validation. **Narinderjit Singh Sawaran Singh:** Methodology, Investigation, Writing – review & editing, Software, Validation. **Sorour Alotaibi:** Methodology, Investigation, Funding acquisition, Formal analysis, Data curation, Conceptualization. **Mahmut Taner:** Methodology, Investigation, Conceptualization, Writing – original draft, Writing – review & editing, Software, Validation. **Shaghayegh Baghaei:** Methodology, Investigation, Funding acquisition. **Soheil Salahshour:** Methodology, Investigation, Funding acquisition, Formal analysis, Data curation, Conceptualization, Writing – original draft, Writing – review & editing, Software, Validation.

Declaration of competing interest

The authors declare that they have no known competing financial interests or personal relationships that could have appeared to influence the work reported in this paper.

Nomenclature

A_m	mushy zone constant (−)
C_p	specific heat (J/kg.K)
g	gravitational acceleration $\left(\mathrm{m}/\mathrm{s}^2\right)$
k	thermal conductivity (W/m·K)
L_f	latent heat (J/kg)
P	pressure (Pa)
Q	heat storage capacity (J)
$\dot{Q}$	heat transfer rate (W)
Re	Reynolds number (−)
S	momentum source term
S_T'''	local thermal entropy generation $\left(\frac{\mathrm{W}}{\mathrm{m}^3.K}\right)$
S_f'''	local frictional entropy generation $\left(\frac{\mathrm{W}}{\mathrm{m}^3.K}\right)$
$\dot{S}_T$	global thermal entropy generation (W/K)
$\dot{S}_f$	global frictional entropy generation (W/K)
T	temperature (K)
t	time (s)
V	velocity (m/s)

Greek symbols

β	thermal expansion coefficient $(1/\mathrm{K})$
λ	liquid fraction (-)
μ	dynamic viscosity (Pa.s)
ρ	density $\left(\mathrm{kg}/\mathrm{m}^3\right)$

Abbreviations

PCM	Phase Change Material
HTF	Heat Transfer Fluid
LHS	Latent Heat Storage
TES	Thermal Energy Storage
STES	Sensible TES

Data availability

No data was used for the research described in the article.

References

Abdollahzadeh, M., Esmaeilpour, M., 2015. Enhancement of phase change material (PCM) based latent heat storage system with nano fluid and wavy surface. Int. J. Heat Mass Tran. 80, 376–385.

Al-Abidi, A.A., Mat, S., Sopian, K., Sulaiman, M.Y., Mohammad, A.T., 2013. Internal and external fin heat transfer enhancement technique for latent heat thermal energy storage in triplex tube heat exchangers. Appl. Therm. Eng. 53, 147–156.

Assis, E., Katsman, L., Ziskind, G., Letan, R., 2007. Numerical and experimental study of melting in a spherical shell. Int. J. Heat Mass Tran. 50, 1790–1804.

Boujelbene, Mohamed, Mohammed, Hayder I., Sultan, Hakim S., Eisapour, Mehdi, Chen, Zhangxin, Mahdi, Jasim M., Cairns, Alasdair, Talebizadehsardari, Pouyan, 2024. A comparative study of twisted and straight fins in enhancing the melting and solidifying rates of PCM in horizontal double-tube heat exchangers. International Communications in Heat and Mass Transfer 151, 107224. https://doi.org/10.1016/j.icheatmasstransfer.2023.107224, 107224. https://linkinghub.elsevier.com/retrieve/pii/S0735193323006139.

Brent, A.D., Voller, V.R., Reid, K.J., 1988. Enthalpy-Porosity technique for modeling convection-diffusion phase change: application to the melting of a pure metal. Numer. Heat Tran. 13 (3), 297–318. https://doi.org/10.1080/10407788808913615.

Choi, J.C., Kim, S.D., 1992. Heat-transfer characteristics of a latent heat storage system using MgCl2· 6H2O. Energy 17, 1153–1164.

Cîrstea, S.D., Moldovan-Teselios, C., Cîrstea, A., Turcu, A.C., Darab, C.P., 2018. Evaluating renewable energy sustainability by composite index. Sustainability 10, 811.

Dehkordi, K.S., Fazilati, M.A., Hajatzadeh, A., 2015. Surface scraped Heat Exchanger for cooling Newtonian fluids and enhancing its heat transfer characteristics, a review and a numerical approach. Appl. Therm. Eng. 87, 56–65.

Dong, X., Jin, X., Li, P., Bi, Q., Gui, M., Wang, T., 2020. Experimental research on heat transfer and flow resistance properties in spiral twisted tube heat exchanger. Appl. Therm. Eng. 176, 115397.

Eisapour, A.H., Eisapour, M., Mohammed, H.I., Shafaghat, A.H., Ghalambaz, M., Talebizadehsardari, P., 2021. Optimum design of a double elliptical latent heat energy storage system during the melting process. J. Energy Storage 44, 103384.

Erek, A., Dincer, I., 2008. An approach to entropy analysis of a latent heat storage module. Int. J. Therm. Sci. 47, 1077–1085.

Guelpa, E., Sciacovelli, A., Verda, V., 2013. Entropy generation analysis for the design improvement of a latent heat storage system. Energy 53, 128–138.

Guo, A.N., Wang, L.B., 2020. The mechanism of laminar convective heat transfer enhancement enforced by twisting of elliptical tube. Int. J. Heat Mass Tran. 157, 119961.

Hajjar, A., Mehryan, S., Ghalambaz, M., 2020. Time periodic natural convection heat transfer in a nano-encapsulated phase-change suspension. Int. J. Mech. Sci. 166, 105243.

Hosseini, M., Rahimi, M., Bahrampoury, R., 2015. Thermal analysis of PCM containing heat exchanger enhanced with normal annular fines. Mech. Sci. 6, 221–234.

Huang, Y., Cao, D., Sun, D., Liu, X., 2022. Experimental and numerical studies on the heat transfer improvement of a latent heat storage unit using gradient tree-shaped fins. Int. J. Heat Mass Tran. 182, 121920.

Huang, Y., Zhai, H., Deng, Z., 2025b. A novel elastic-driven phase-change thermal buffer for efficient thermal management. Int. J. Heat Mass Tran. 239, 126586.

Huang, Y., Zhang, C., Chen, Y., 2025a. Rapid charging and discharging strategies for latent heat storage. Renew. Sustain. Energy Rev. 222, 115953.

Jourabian, M., Darzi, A.A.R., Akbari, O.A., Toghraie, D., 2020. The enthalpy-based lattice Boltzmann method (LBM) for simulation of NePCM melting in inclined elliptical annulus. Phys. A Stat. Mech. its Appl. 548, 123887.

Jourabian, M., Farhadi, M., Rabienataj Darzi, A.A., 2016. Heat transfer enhancement of PCM melting in 2D horizontal elliptical tube using metallic porous matrix. Theor. Comput. Fluid Dynam. 30, 579–603.

Jourabian, M., Farhadi, M., Sedighi, K., Darzi, A.A.R., Vazifeshenas, Y., 2012. Melting of NEPCM within a cylindrical tube: numerical study using the lattice Boltzmann method. Numer. Heat Tran. 61 (12), 929–948.

Kalapala, L., Devanuri, J.K., 2018. Influence of operational and design parameters on the performance of a PCM based heat exchanger for thermal energy storage–A review. J. Energy Storage 20, 497–519.

Kashani, S., Ranjbar, A., Abdollahzadeh, M., Sebti, S., 2012. Solidification of nano-enhanced phase change material (NEPCM) in a wavy cavity. Heat Mass Tran. 48, 1155–1166.

Khedher, Nidhal Ben, Mahdi, Jasim M., Dulaimi, Anmar, Chatroudi, Ilia Shojaeinasab, Ebrahimnataj Tiji, Mohammadreza, Ibrahem, Raed Khalid, Yvaz, A., Talebizadehsardari, Pouyan, 2023. On the application of novel arc-shaped fins in a shell-and-tube type of latent heat storage for energy charge enhancement. Journal of Energy Storage 73, 108697. https://doi.org/10.1016/j.est.2023.108697, 108697. https://linkinghub.elsevier.com/retrieve/pii/S2352152X23020947.

Khedher, Nidhal Ben, Mohammed, Hayder I., Abed, Azher M., Biswas, Nirmalendu, Togun, Hussein, Hammoodi, Karrar A., Mahdi, Jasim M., Talebizadehsardari, Pouyan, 2025. Maximizing charging/discharging capabilities of horizontal shell-and-tube latent heat storage systems with innovative curved fin inserts. International Journal of Heat and Mass Transfer 236, 126289. https://doi.org/10.1016/j.ijheatmasstransfer.2024.126289, 126289. https://linkinghub.elsevier.com/retrieve/pii/S0017931024011189.

Khedher, Nidhal Ben, Togun, Hussein, Aljibori, Hakim S. Sultan, Mohammed, Hayder I., Khosravi, Koorosh, Abed, Azher M., Boujelbene, Mohamed, Mahdi, Jasim M., 2024. Accelerated melting dynamics in latent-heat storage systems via longitudinal and circular fins: A comprehensive 3D analysis. International Communications in Heat and Mass Transfer 156, 107602. https://doi.org/10.1016/j.icheatmasstransfer.2024.107602, 107602. https://linkinghub.elsevier.com/retrieve/pii/S0735193324003646.

Khoshvaght-Aliabadi, M., Deldar, S., Rehman, S., Alimoradi, A., 2021. Comparative study of heat transfer and pressure drop for curved-twisted tubes utilized in chemical engineering. Chin. J. Chem. Eng. 40, 53–64.

Li, X., Wang, L., Feng, R., Wang, Z., Liu, S., Zhu, D., 2021. Study on shell side heat transport enhancement of double tube heat exchangers by twisted oval tubes. Int. Commun. Heat Mass Tran. 124, 105273.

Li, Z., Shahsavar, A., Niazi, K., Al-Rashed, A.A.A.A., Talebizadehsardari, P., 2020. The effects of vertical and horizontal sources on heat transfer and entropy generation in an inclined triangular enclosure filled with Non-Newtonian fluid and subjected to magnetic field. Powder Technol. 364, 924–942.

Li, Z.X., Al-Rashed, A.A.A.A., Rostamzadeh, M., Kalbasi, R., Shahsavar, A., Afrand, M., 2019. Heat transfer reduction in buildings by embedding phase change material in multi-layer walls: effects of repositioning, thermophysical properties and thickness of PCM. Energy Convers. Manag. 195, 43–56.

López-Núñez, O.A., Alfaro-Ayala, J.A., Jaramillo, O., Ramírez-Minguela, J., Castro, J.C., Damian-Ascencio, C.E., Cano-Andrade, S., 2020. A numerical analysis of the energy and entropy generation rate in a Linear Fresnel Reflector using computational fluid dynamics. Renew. Energy 146, 1083–1100.

Lotfi, B., Sundén, B., Wang, Q., 2016. An investigation of the thermo-hydraulic performance of the smooth wavy fin-and-elliptical tube heat exchangers utilizing new type vortex generators. Appl. Energy 162, 1282–1302.

Luo, C., Song, K.W., 2021. Thermal performance enhancement of a double-tube heat exchanger with novel twisted annulus formed by counter-twisted oval tubes. Int. J. Therm. Sci. 164, 106892.

Mahdi, J.M., Lohrasbi, S., Ganji, D.D., Nsofor, E.C., 2018. Accelerated melting of PCM in energy storage systems via novel configuration of fins in the triplex-tube heat exchanger. Int. J. Heat Mass Tran. 124, 663–676.

Mahdi, J.M., Lohrasbi, S., Ganji, D.D., Nsofor, E.C., 2019. Simultaneous energy storage and recovery in the triplex-tube heat exchanger with PCM, copper fins and Al2O3 nanoparticles. Energy Convers. Manag. 180, 949–961.

Mahdi, J.M., Nsofor, E.C., 2018. Solidification enhancement of PCM in a triplex-tube thermal energy storage system with nanoparticles and fins. Appl. Energy 211, 975–986.

Nguyen, T.K., Sheikholeslami, M., Shehzad, S.A., Shafee, A., Alghamdi, M., 2019. Solidification entropy generation via FEM through a porous storage unit with applying a magnetic field. Phys. Scri. 94, 095207.

Pizzolato, A., Sharma, A., Maute, K., Sciacovelli, A., Verda, V., 2017. Design of effective fins for fast PCM melting and solidification in shell-and-tube latent heat thermal energy storage through topology optimization. Appl. Energy 208, 210–227.

Sardari, P.T., Giddings, D., Grant, D., Gillott, M., Walker, G.S., 2019. Discharge of a composite metal foam/phase change material to air heat exchanger for a domestic thermal storage unit. Renew. Energy 148, 987–1001.

Shahsavar, A., Majidzadeh, A.H., Mahani, R.B., Talebizadehsardari, P., 2021. Entropy and thermal performance analysis of PCM melting and solidification mechanisms in a wavy channel triplex-tube heat exchanger. Renew. Energy 165, 52–72.

Shokouhmand, H., Kamkari, B., 2012. Numerical simulation of phase change thermal storage in finned double-pipe heat exchanger. Proc. Applied Mechanics and Materials. Trans Tech Publ, pp. 742–746.

Song, Y.-Q., Izadpanahi, N., Fazilati, M.A., Lv, Y.-P., Toghraie, D., 2021. Numerical analysis of flow and heat transfer in an elliptical duct fitted with two rotating twisted tapes. Int. Commun. Heat Mass Tran. 125, 105328.

Talebizadehsardari, P., Mahdi, J.M., Mohammed, H.I., Moghimi, M., Eisapour, A.H., Ghalambaz, M., 2021. Consecutive charging and discharging of a PCM-based plate heat exchanger with zig-zag configuration. Appl. Therm. Eng. 193, 116970.

Wang, P., Wang, X., Huang, Y., Li, C., Peng, Z., Ding, Y., 2015. Thermal energy charging behaviour of a heat exchange device with a zig-zag plate configuration containing multi-phase-change-materials (m-PCMs). Appl. Energy 142, 328–336.

Wang, W.-W., Wang, L.-B., He, Y.-L., 2016. Parameter effect of a phase change thermal energy storage unit with one shell and one finned tube on its energy efficiency ratio and heat storage rate. Appl. Therm. Eng. 93, 50–60.

Xu, Y., Ren, Q., Zheng, Z.-J., He, Y.-L., 2017. Evaluation and optimization of melting performance for a latent heat thermal energy storage unit partially filled with porous media. Appl. Energy 193, 84–95.

Yan, S., Fazilati, M.A., Toghraie, D., Khalili, M., Karimipour, A., 2021. Energy cost and efficiency analysis of greenhouse heating system enhancement using phase change material: an experimental study. Renew. Energy 170, 133–140.

Yang, X., Lu, Z., Bai, Q., Zhang, Q., Jin, L., Yan, J., 2017. Thermal performance of a shell-and-tube latent heat thermal energy storage unit: role of annular fins. Appl. Energy 202, 558–570.

Ye, W.-B., Zhu, D.-S., Wang, N., 2011. Numerical simulation on phase-change thermal storage/release in a plate-fin unit. Appl. Therm. Eng. 31, 3871–3884.

Yu, C., Cui, Y., Zhang, H., Gao, B., Zeng, M., Han, L., 2022. Comparative study on turbulent flow characteristics and heat transfer mechanism of a twisted oval tube with different twisted tapes. Int. J. Therm. Sci. 174, 107455.

Yuan, Y., Cao, X., Xiang, B., Du, Y., 2016. Effect of installation angle of fins on melting characteristics of annular unit for latent heat thermal energy storage. Sol. Energy 136, 365–378.